RESEARCH ARTICLE



How side-chain hydrophilicity modulates morphology and charge transport in mixed conducting polymers

Aditi Khot | Brett M. Savoie (1)

Davidson School of Chemical Engineering, Purdue University, West Lafayette, Indiana, USA

Correspondence

Brett M. Savoie, Davidson School of Chemical Engineering, Purdue University, West Lafayette, IN 47906, USA. Email: bsavoie@purdue.edu

Funding information

Electrochemical Systems Program, Grant/ Award Number: 2045887-CBET

Abstract

Organic mixed ionic-electronic conductors (OMIECs) are a developing class of organic electronic materials distinguished by their dual modes of conduction. The side-chains of OMIEC polymers are responsible for forming a percolating electrolyte phase that mediates doping and ionic conduction. Despite this critical role, design rules for OMIEC side-chains are still nascent and their effects on OMIEC morphology and charge transport have yet to be systematically studied. Here we perform the first dedicated coarse-grained molecular dynamics study of OMIECs where the side-chain identity and distribution are systematically varied using a random copolymer architecture. The simulations recapitulate the nonlinear progression of the morphology from an interfacially gated electrolyte when large fractions of hydrophobic side-chains are incorporated, to an electrolyte swelled morphology after crossing a threshold of approximately 40% polar side-chains. Kinetic Monte Carlo simulations were used to characterize the charge transport behaviors in these systems, revealing two interesting maxima in the mobility at 40% and 100% polar side-chain fractions, respectively. With respect to maximizing the charge mobility and conductivity, these simulations suggest that a uniform hydrophilic side-chain distribution is optimal and that there are few advantages to using mixed side-chains in a random copolymer architecture. These results also suggest several alternative side-chain engineering strategies for optimizing OMIEC performance.

KEYWORDS

charge transport, mixed conduction, polymer electrolytes, polymer semiconductors

1 | INTRODUCTION

Organic mixed ionic-electronic conductors (OMIEC)¹ are composed of organic semiconducting polymers and an absorbed electrolyte. OMIECs exhibit electron conduction within the polymeric phase while ionic conductivity is mediated by a percolating electrolyte phase. Depending on the degree of mixing and polymer characteristics, these two conduction channels can be strongly coupled, with ion percolation leading to volumetric doping of the

polymer. This mechanism has been exploited for signal transduction and charge storage, and is the basis for several technologies, including organic batteries and super capacitors,^{2–4} organic electrochemical transistors,⁵ neurocomputing devices^{5–7} light-emitting electrochemical cells,⁸ chemical sensors,⁹ and electrochromic devices.¹⁰

Given the extensive prior work on developing organic semiconductors (OSC), a common OMIEC design strategy is to add polar side-chains (e.g., glycol derivatives) to extant p-type^{11–13} and n-type^{13–16} OSCs to enable electrolyte

percolation and doping. In contrast, the alkylic sidechains typically used in OSC applications do not enable electrolyte percolation and these materials only exhibit limited interfacial doping rather than mixed conduction when interfaced with an electrolyte. 11 Additionally, polar side-chains facilitate co-processing of polymer with dopants¹² and decrease ion aggregation. 12,16 Nevertheless, replacing the side-chains of OSCs potentially leads to adverse morphological changes with respect to charge transport and the optimal strategy for selecting sidechains is unknown. Likewise, the actual morphology that governs mixed conduction is substantially influenced by the details of the electrolyte and the degree of percolation, and the features that constitute an optimal (or at least acceptable) OMIEC morphology are still being resolved.

In the past few years, extensive efforts have been dedicated to developing OMIECs specifically for organic electrochemical transistors (OECT).5 For this reason, the structure-function relationships that have been observed for side-chain engineering of OMIECs have been studied in the context of OECTs. In an OECT, the output sourcedrain current is the current through the polymer film, which is modulated by changing the doping within the polymer via a gate electrode in the electrolyte. The magnitude of the current change is related to the transconductance—the product of capacitance carrier mobility—of the OMIEC and is thus a key figureof-merit.¹⁷ However, relating transconductance to sidechain identity is complicated by how doping efficiency (i.e., carriers created in the polymer per electrolyte dopant) and carrier mobility potentially respond to increased electrolyte uptake. For example, increased electrolyte uptake straightforwardly increases capacitance, while it has an indeterminant effect on doping efficiency and mobility. Several comparative studies of how side-chain chemistry impacts OECT performance have documented a variety of behaviors depending on the polymer chemistry, electrolyte, and particular side-chain substitution. Two recent studies investigated how OECT properties respond to incorporating varying amounts of polar and apolar side-chains on different OMIEC polymer backbones. 18,19 For both p-type and n-type conducting polymers, these studies observed that all polar side-chains generally maximize the transconductance. Both studies observed maximum electrolyte uptake for the all polar side-chain cases, suggesting that the net increase in doping offsets any potentially negative effects on doping efficiency or mobility. The side-chain length, branching, frequency, and placement have also been shown to affect OMIEC figures of merit. These factors have been explored for specific backbone and electrolyte combinations across many recent experimental studies, 15,20-30 and

to a lesser extent by simulations. 31,32 Among the salient trends from these studies, are that branched side-chains exhibit higher capacitance²⁰ but lower conductivity,²¹ intermediate length side-chains (3 glycol units) lead to the highest transconductance. 21,23 and tail-to-tail sidechain linkage shows higher transconductance than headto-head linkage.²⁴ An additional strategy that has recently gained traction is to include an alkyl linker between polar side-chains and the backbone to limit backbone-electrolyte interactions and improve polymer packing and conductivity.^{25–29} However, these side-chain design rules are not universal and strongly depend on the backbone chemistry. 15,30 Since the transconductance is proportional to the product of the mobility and carrier concentration, it is expected that several of these trends are dominated by the increase in net doping that occurs when including more polar side-chains, which also compensates for the potential decreases of mobility or doping efficiency that might occur upon polymer swelling by the electrolyte. However, the molecular details of these competing trends and the degree to which mobility and doping efficiency might be simultaneously optimized with electrolyte uptake remain undetermined.

To provide molecular insight into some of these potential trade-offs, we have performed the first molecular dynamics (MD) study of the effect of systematically varying the side-chain polarity on the morphology and mixed conduction of a model OMIEC based on a thiophene backbone with either alkyl or glycolated sidechains. A generic computational framework for coarsegrained molecular dynamics (CG-MD) and kinetic Monte Carlo (KMC) simulations is used for this purpose that was recently developed by our group.³³ These simulations provide molecular level details on electrolyte percolation, morphology, and charge transport to supplement the macroscopic picture that has been previously established in experimental studies. Additionally, this study validates that our model correctly captures the effect of side-chain design variables to the extent that experimental comparisons are possible, and opens the door for future sidechain design studies.

2 | METHODS

The coarse-grained force field and KMC framework used here for modeling OMIECs was recently reported and benchmarked in a separate publication by the authors.³³ In the following sections, we briefly review the details and highlight the changes with respect to the originally reported implementation. In the Appendix S1, all force field parameters and simulation conditions are reported to facilitate reproducibility of the simulations.

2.1 | Coarse-grained model

The OMIEC MD model used in this study was composed of an anisotropic conjugated backbone, and isotropic side-chain, ions, electrolyte solvent, and a processing solvent. Unless specified otherwise, the isotropic bonded and nonbonded interactions refer to bead types from Martini version 2.^{34,35} To better approximate film processing, all simulations were first equilibrated in chloroform, modeled by a C4 Martini bead, followed by equilibration in an aqueous electrolyte modeled using a chloride counter-ion and coarse-grained water. The polarizable Martini force field was used for water, ³⁵ and chloride ions were represented by a Qa bead.

A comparison of polar and apolar side-chains was performed using isotropic Martini-based beads that are representative of alkyl and polyethylene glycol (PEG) chains, respectively, which are commonly used side-chains in experiments. The alkyl side-chain was modeled with the SC3 Martini bead that represents a propyl group (Figure 1) as has previously been implemented in the Martini model of poly(3-hexyl thiophene) (P3HT).36 For the PEG chain, we adopted the parameters from the Martini CG model for polyethelyene glycol,³⁷ where an EO bead represents the CH2 – O – CH2 group (Figure 1). However, the EO bead was originally parameterized with the water force field from Martini version 2.2. To make it compatible with the polarizable water model, we modified the interaction of EO with the POL water bead by setting $\varepsilon = 3.325 \text{ kJ/mol}$, to obtain a hydration free energy of -14.77 kJ/mol,

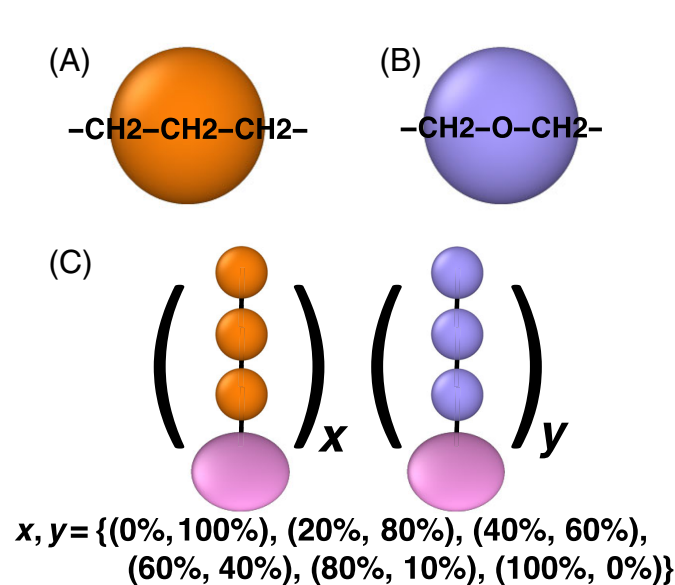


FIGURE 1 The coarse-grained mapping of the apolar (A) and polar (B) beads used to model the hydrophobic and hydrophilic polymer side-chains, respectively. (C) The materials simulated here consist of random copolymers with varying fractions of the two types of side-chain

which is comparable to the value of $-14.73~\rm kJ/mol$ obtained by the original Grunewald model. The bonded parameters for EO were also retained from the Grunewald model except for the restricted bending potential and instead cosine-squared potential was used similar to the original Martini model. As the purpose of the restricted-bonding potential was numerical stability and we are modeling short PEG oligomers as side-chains, this modification should be inconsequential.

As in our previous work, the potential interaction between backbone beads was modeled using an anisotropic Gay-Berne potential³⁸ and the orientation of consecutive backbone beads was controlled using additional torsional and stretching potentials.33 The Gay-Berne potential parameters were selected to be representative of thiophene and follow our previous report. Simulations of a 3-hexylthiophene (3HT) monomer liquid based on this backbone and two SC3 side-chain beads (i.e., the same Martini model that has previously been used for P3HT³⁶) resulted in a density of 0.97 g/cc that was in close agreement with the experimental density of 0.95 g/cc. The backbone bonded potential parameters were modified to obtain a persistence length of 7.34 repeat units (RU) for P3HT in toluene, comparable to the experimental persistence length for polythiophene of 6.75–7.43 RU.³⁹ As in our previous work, the backbone bead interacts with other side-chain and solvent beads with an isotropic potential, but is modeled as a Martini C4 bead here instead of a C3 bead from our previous model. The Martini C4 bead reproduces the hexadecane-water partition free energy of a thiophene ring as 9.27 kJ/mol in better agreement than C3 with the experimental partition free energy of 10 kJ/mol 40

All simulations consisted of monodisperse solutions containing polymers of 50 backbone beads. Six polymer compositions were studied (Figure 1C) with varying amounts of polar and apolar side-chains: 0% polar (100% apolar), 20% polar (80% apolar), 40% polar (60% apolar), 60% polar (40% apolar), 80% polar (20% apolar), and 100% polar (0% apolar). Each side-chain contained 3 CG beads representing roughly 9 heavy atoms. The side-chains were attached on each backbone bead in a regioregular fashion. The cases with mixed amounts of polar and apolar side-chains were modeled as random copolymers by stochastically assigning the identity of each side-chain. The degree of polymerization^{25,41} and side-chain length^{11,14,23} were selected to be comparable to that of typical experimental OMIECs.

2.2 | Molecular dynamics

LAMMPS was used to perform all MD simulations.⁴² All simulations used a 10 fs integration time step,

Velocity-Verlet integration, and periodic boundary conditions. Lennard-Jones, electrostatic, and Gay-Berne interactions were truncated at 12 Å. The Lennard-Jones and Coulombic interactions were shifted using the standard GROMACS shift function over a length of 9–12 Å and 0–12 Å, respectively. Film equilibration occurred over two distinct simulations. First, polymer film formation was simulated by dissolving the neutral polymers in chloroform then evaporating the solvent. Subsequently, the polymers were doped (i.e., charged) and electrolyte was added to the simulation and allowed to equilibrate.

For the polymer film formation simulations, the polymer and chloroform solvent molecules were initialized from diffuse configurations, using a cubic grid to place molecules in random orientations without overlap. Each simulation box contained 50 polymers and was initially surrounded by 50,000 chloroform molecules. The velocities were initialized from a uniform distribution obtained with a random seed value and scaled to give the correct kinetic energy. The simulations were first relaxed in the NVE ensemble with restrained displacements of 0.1 Å per time step for 10 ps. This was followed by a simulation in the NVT ensemble at 300 K while linearly rescaling the simulation box over 2 ns to obtain a condensed system with a density of 1 g/cc. The density was then equilibrated in the NPT ensemble for 100 ns at 300 K and 1 atm. After the NPT simulation, 20 wt% of the chloroform beads were randomly selected and removed from the system, followed by an equilibration step in the NPT ensemble for 100 ns at 300 K and 1 atm. This process of chloroform removal followed by NPT equilibration was performed five times, resulting in 28,750 (80 wt% of solvent), 10,781 (60%), 4792 (40%), 1797 (20%), and 0 (0%) chloroform molecules, respectively. This procedure is intended to qualitatively mimic the solvent processing and evaporation during experimental film formation (e.g., spin-coating) and has been employed in other coarse-grained simulations of organic polymers.43

The final polymer film configuration was unwrapped in accordance with the periodic boundary conditions, the backbone beads were charged and then surrounded by randomly placed solvent and ion beads on the outside of the polymer film, each within a separate cubic box of length 6 Å to avoid overlaps. At this stage, 10,781 CG water beads were added, which correspond to 43,124 real water molecules and 60 wt% of solvent. Each backbone unit carried a charge of +0.2 (i.e., a doping induced charge every five backbone beads), and 500 counter-ions with a charge of -1.0 were added to achieve charge neutrality. These systems were relaxed in the NVE ensemble with restrained displacements of 0.1 Å per time step for

10 ps, followed by an NPT equilibration for 100 ns, and an NPT production run for an additional 100 ns at 300 K and 1 atm. In all of the NVT and NPT simulations, the Nosé-Hoover thermostat and barostat were employed using the modified form proposed by Martyna, Tobias, and Klein, as implemented in LAMMPS, 44 with a relaxation time constant of 0.15 and 1.5 ps for the thermostat and barostat, respectively. In all of the simulations, the thermodynamic data and coordinates were sampled at 1 ps. The ASPHERE package in LAMMPS was used for all Gay-Berne force evaluations, torque evaluations, and numerical integrations.⁴⁵ The SHAKE algorithm⁴⁶ implemented as a part of the RIGID package in LAMMPS was used to constrain the bonds in the water molecules. Additional bonded potentials to control the orientation of neighboring beads were implemented as custom classes in LAMMPS by our group. OVITO was used for visualizing the final trajectories and generating snapshots of MD configurations.47

2.3 | Charge transport calculations

Charge transport within the OMIEC polymer network was modeled on the basis of configurations generated from the CG-MD trajectories. The expressions for charge transport rates, the physics behind the rate parameters, the choice of these rate parameters, the KMC procedure, and the final calculation of mobility was explained in detail in our previous work.³³ In brief, each backbone bead was parameterized to represent a single conjugated unit (i.e., a ring system without internal flexible dihedral degrees of freedom); thus, sites consisting of one or more contiguous backbone beads constitute the relevant polaronic basis states for charge transfer. The extent of polaron delocalization (i.e., the number of contiguous beads involved in a single polaron site) was determined based on a threshold for the charge transfer rate for contiguous beads (10¹⁴s⁻¹). Contiguous beads with charge transfer rates above this threshold were combined together to form a delocalized polaron site; contrarily, smaller polaron sites reflect poor torsional alignment or electrostatic disorder along the polymer chains. The charge transfer rates between polaron sites were parameterized using semi-classical Marcus theory, 48 whereas the charge transport between contiguous beads was modeled using a modified Marcus rate in the adiabatic limit.49,50 The charge transfer rate parameters capture the appropriate dependence on the delocalization of electrons along the backbone, the electronic coupling due to orbital overlap, the reorganization energy in the presence of solvent, and the energetic disorder due to electrostatic interactions with the solvent.

The expression used to calculate the intermolecular electronic coupling was updated to be calculated on the basis of individual pairwise couplings between beads, instead of an average intersite distance over all beads, as was done previously. The new expression for coupling is

$$J_{ij} = J_{\text{inter}} \sum_{m \in i \cup j} \exp\{-\alpha (r_{\min,m} - r_0)\}, \tag{1}$$

where α is a decay factor, r_0 is the reference separation for J_{inter} , and $r_{m,min}$ is the minimum distance of bead m in site i (or j) from beads in the other site j (or i). This expression defines the coupling between backbone units and assigns a nonzero coupling for polymers that partially overlap, which was not captured by the earlier expression based on the average intersite distance. The intermolecular coupling value J_{inter} , the reference separation r_0 , and the decay factor α were set to 0.01 eV, 3.5 Å and 0.8 Å^{-1} , respectively to match with the new coupling expression and commonly reported values in organic electronic literature.⁵¹ The values for HOMO energy levels and reorganization energy as a function of site length were obtained from the length-dependence study by Zade et al. on polythiophenes.⁵² The intramolecular reference coupling, J_{intra} , used in the adiabatic rate expression for charge transfer between contiguous beads was set to a value of 0.31 eV. This parameter raises or lowers the mean intrachain charge transfer rates and thus affects the delocalization length of the polaron sites. Here, J_{intra} was selected to obtain an average polaron delocalization length of \sim 13 backbone beads for the 100% polar side-chain case (Figure 4). The delocalization lengths ranged from 1 to 50 (polarons localized to a single backbone bead vs the entire polymer chain) depending on the side-chain composition, degree of backbone order, and local electrostatic interactions with electrolyte.

A common numerical problem in KMC simulations of processes with kinetics spanning multiple orders of magnitude, is that the slow processes are necessarily rarely sampled. In the current systems, intrachain charge transfer rates tend to be much larger than interchain rates, with the effect that the charge can spend a large number of KMC steps hopping within a small set of spatially localized sites while waiting for a relatively slow interchain hop to occur. To address this problem, we use the Aggregate Monte Carlo (AMC) procedure proposed by Brereton et al.⁵³ In the AMC procedure, polaron sites are aggregated together based on their connectivity and relatively high rates for transfer, then the charge transport is simulated similar to KMC as a Markov chain of jumps between these aggregates. An important distinction is that the transport out of an aggregate is modeled as a Markov jump process from the trap to any of its neighbors which are treated as absorbing barriers. In doing this, the time spent in the trap site is correctly accounted for and the exit probabilities depend on the transport probability to the neighbors as well as the transport within the trap region. In order to determine the aggregates, we use the decomposition algorithm described in Brereton et al with the hyperparameters $\alpha = 0.2$, $\beta = 0.2$ and $\gamma = 0.03$.⁵³

The key steps involved in the charge transport characterization are summarized below. For each configuration sampled at time *t* obtained from the CG-MD simulation,

- 1. Calculation of intramolecular rates: The charge transfer rates between contiguous backbone beads are calculated in preparation for defining polaron sites. These rates are averaged over 20 configurations over $t\pm 1$ ps.
- 2. Definition of polaronic basis states: The contiguous beads with rates above 10^{14} s⁻¹ are combined into a single site.
- 3. Calculation of intermolecular rates: The charge transfer rates between polaron sites are averaged over 20 configurations uniformly sampled from $t\pm 1$ ps.
- 4. Determination of Aggregate States: Polaron sites with fast transfer rates are aggregated and their exit probabilities are calculated based on the decomposition algorithm.
- 5. KMC simulations of charge hopping trajectories: For each configuration, 40 trajectories are generated by randomly choosing different starting sites.

The above procedure to generate polaron transport trajectories were performed for 20 configurations sampled every 5 ns and subsequently, the diffusivity and mobility were estimated from the mean squared displacement (MSD) of the polaron. The MSD and mobility calculation was performed for three independent MD simulations to obtain the net average mobility and error reported below. Likewise, distributions of various quantities such as electronic coupling, energies, site length, etc. were obtained as averages over the three independent MD simulations.

3 | RESULTS AND DISCUSSION

3.1 | Morphology characterization

The simulated series of OMIECs comprise a case study on the effects of varying the side-chain hydrophilicity and composition on the morphology and transport of random copolymers. We first focus on the distinct morphological features across the series, since it provides an interpretive basis for the later charge transport results.

The density of polar side-chains has a predictably large impact on the extent of electrolyte percolation in

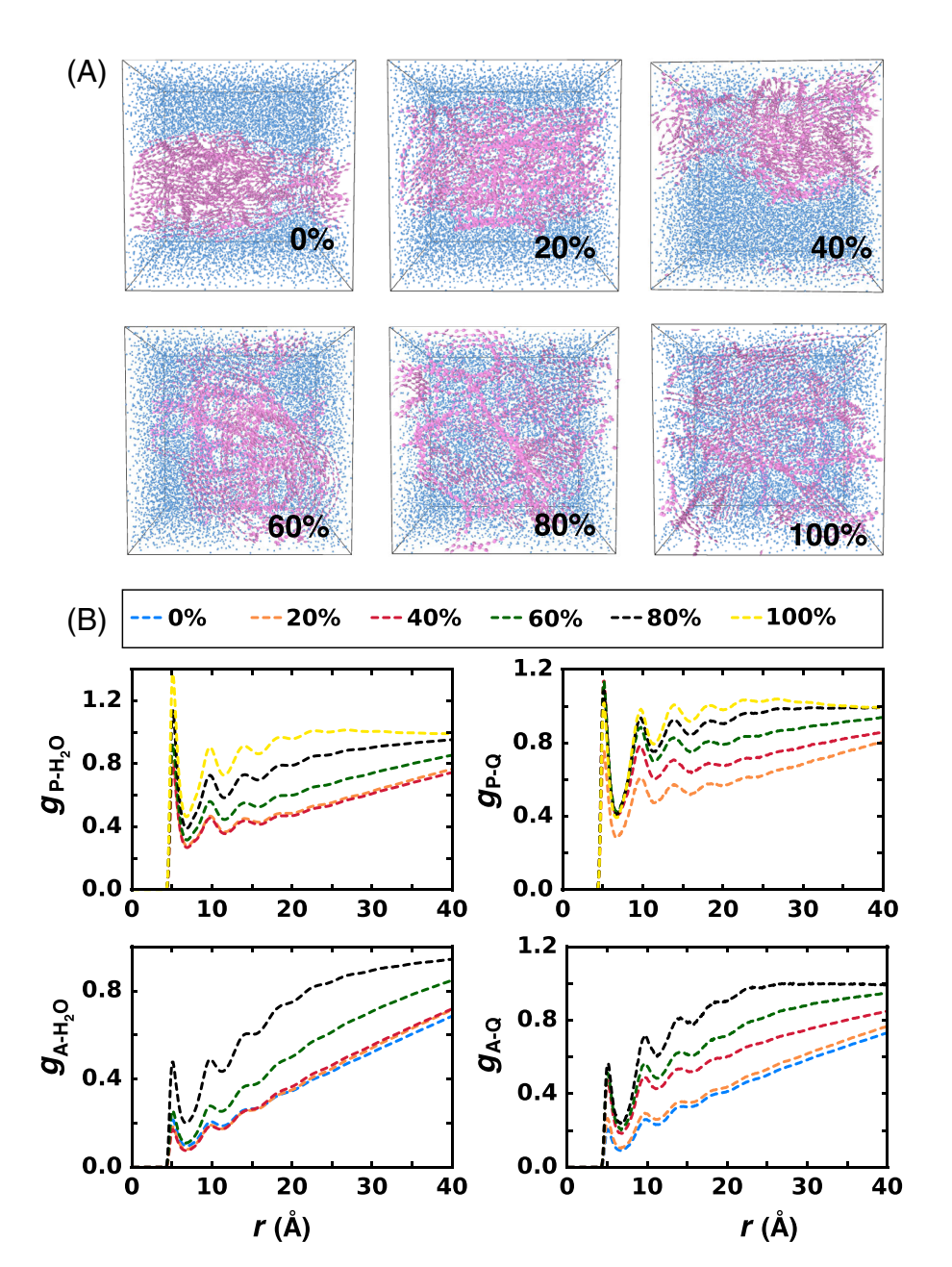


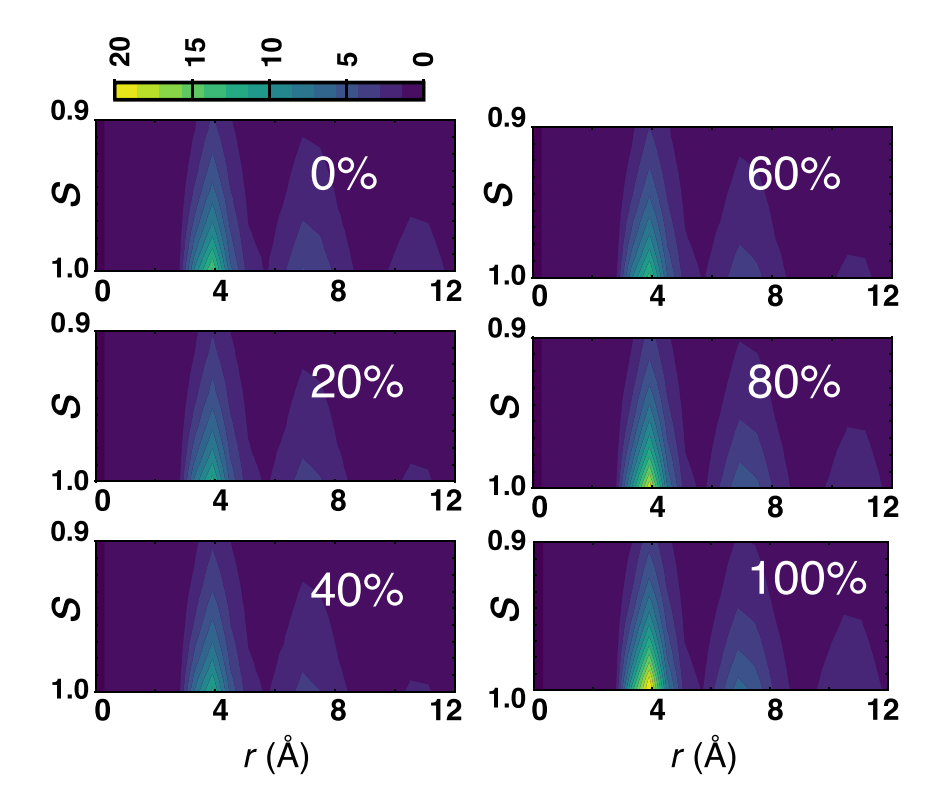
FIGURE 2 (A) Snapshots showing polymer (pink) and water (blue) for different side-chain compositions. All other bead types are omitted for clarity. (B) Radial distribution functions g_{x-y} for the polar side-chains and water (P-H₂O), polar side-chains and ions (P-Q), apolar side-chains and water (A-H₂O), and apolar side-chains and ions (A-Q)

each OMIEC. Representative snapshots for each system demonstrate the onset of electrolyte percolation around 40%–60% of polar side-chain incorporation (Figure 2). The trend is notably nonlinear, as the morphology qualitatively changes from a relatively dense organic film with excluded electrolyte to a swelled network around a concentration of 60% polar side-chains. Neglecting other factors, the free energy of water absorption should be linear in the fraction of polar side-chains, meaning that the likelihood of water percolation would be exponential in the polar fraction. This is consistent with the apparent phase transition around 60% polar side-chain fraction, and also consistent with experimental observations of super-linear swelling with respect to the fraction of polar side-chains. ^{18,19} For the simulated electrolyte densities, a bulk

electrolyte phase persists until $\geq 80\%$ hydrophilic sidechain fractions, at which point the polymers completely swell (Additional details can be observed in Figure S2).

The side-chain composition also has several subtle effects on the distribution of electrolyte within the polymer phase (Figure 2). First, the much larger probabilities for finding water and ions near polar side-chains compared with apolar side-chains (Figure 2B) confirms the intuition that the former drive electrolyte percolation within the OMIEC. We also observe that the effective (a)polarity of the side-chains is a function of side-chain concentration. Specifically, as the fraction of polar chains increases, the likelihood of finding water and ions near the apolar chains also increases. Conversely, as the fraction of apolar chains increases the

FIGURE 3 $\pi - \pi$ stacking probability presented as a joint probability distribution of distance between the backbone beads on the *x*-axis and $\pi - \pi$ alignment on the *y*-axis, as a function of polymer side-chain composition



likelihood of observing electrolyte near the polar chains decreases. At polar fractions $\leq 40\%$ this is explainable by limited electrolyte percolation, which correspondingly limits electrolyte association with buried polar chains. However, this trend is also observable in the percolating morphologies, which we interpret to reflect the effect of neighboring side-chains on the local hydrophilicity. Specifically, at higher polar side-chain fractions, both polar and apolar side-chains are more likely to have a polar neighbor that promotes local association with the electrolyte. The reverse is also true as the fraction of apolar chains increases. It is not obvious whether this effect is immediately useful, but it is a distinct prediction of the simulations and we would hypothesize that it is more pronounced in random copolymers (as simulated here), compared with block copolymers.

A key feature of the employed OMIEC model is that it explicitly describes the π -orientation of the polymer backbone. The $\pi-\pi$ organization between chains was characterized using the joint-distribution function of backbone bead separation and the dot product of the π normal vectors, S (Figure 3). All of the systems exhibit a high degree of $\pi-\pi$ organization (i.e., S>0.8 in all cases) between neighboring chains; however, in the progression from low to high polar side-chain fraction, we observe that the $\pi-\pi$ organization decreases for intermediate fractions ($\geq 20\%$) of polar side-chains. We ascribe this to the combination of side-chain heterogeneity and partial percolation of the electrolyte, both of which frustrate

chain packing at the intermediate fractions. This trend is also consistent with the organization at the second and third nearest neighbor chain positions (i.e., \sim 7 and 11 Å, respectively). Interestingly, the 100% polar case with the greatest degree of electrolyte swelling shows the highest overall organization. In contrast, the 100% apolar case shows weaker organization, but we caution that this system forms a thin layer (5 nm) that is dominated by the polymer-electrolyte interface and is not representative of a bulk organic semiconducting polymer. The onedimensional radial distribution functions for the backbone beads also reveal several subtle features (Figure S2d). For instance, there is only weak lamellar organization as evidenced by a small peak at \sim 17 Å that is suppressed with increasing electrolyte percolation.⁴¹ This length is consistent with experimentally reported length of 14-19 Å, 14,19,41 roughly two times the side-chain length, and thus also indicates that limited side-chain interdigitation occurs in these systems.

3.2 | Charge transport characterization

Next, we examined how charge transport within the polymer is affected by the changes in morphology and electrostatic environment attendant to changing the sidechain composition. Charge transport was modeling using KMC to generate ensembles of single polaron hopping trajectories across a range of representative MD

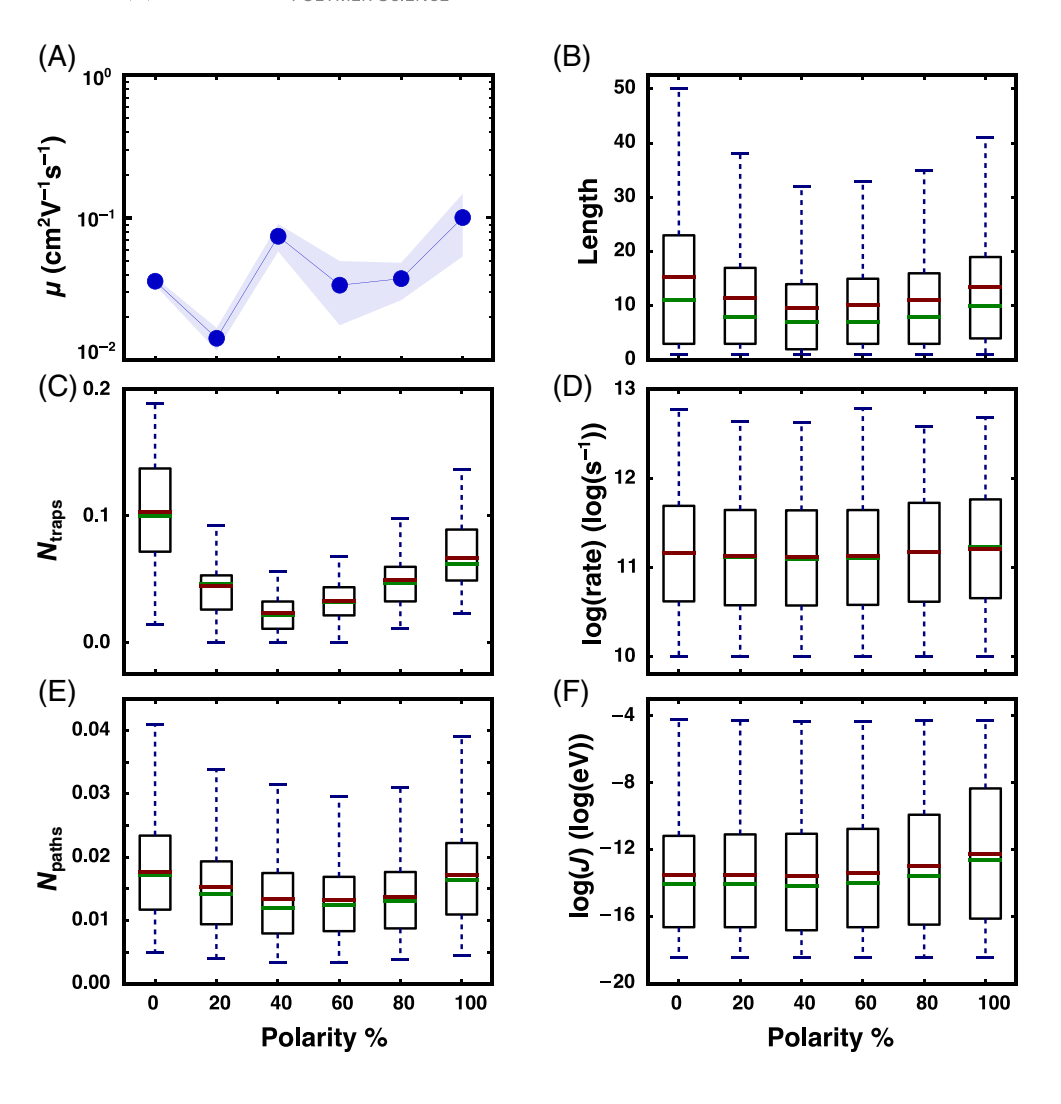


FIGURE 4 (A) Charge mobility, (B) polaron delocalization length (number of backbone beads per polaron site), (C) number of trap sites $(N_{\rm traps})$ normalized by total number of aggregated sites, (D) log distribution of the intersite charge transfer rate, (E) the number of pathways per site (N_{paths}) normalized by the total number of pathways, and (F) log distribution of the intersite electronic coupling, across different side-chain compositions. The green and red lines in the whisker plots indicate the median and mean, respectively

configurations for each system. The mobilities extracted from these simulations reflect the low carrier density limit and do not capture potential finite-concentration effects (e.g., trap filling). The interpretive advantage of the low-density limit is that the mobility changes solely reflect the changes in morphology and energy distribution. We note that finite-concentration simulations are compatible with the KMC approach, but consider a comparison in the context of OMIECs to be beyond the current scope.

The trend in simulated polaron mobilities shows an increase for the cases with electrolyte percolation (≥40%), and a maximum for the 40% and 100% polar side-chain fractions (Figure 4). Nevertheless, these trends are minor in comparison with the similar order of magnitude of the mobility in all of the cases. Experimentally, the electronic mobility generally increases with polar side-chain concentration, but a direct comparison is difficult since the experimental charge carrier densities generally increase with polar side-chain concentration rather than remaining fixed as simulated here. ^{18,19} Considering that the mobility typically increases with respect to increasing

charge density, the present prediction of relatively constant mobility in the low carrier density limit as the polar side-chain fraction increases is broadly consistent with the experimental trend.

We note that the error bars illustrate the variance across the simulated KMC trajectories, but there is also uncertainty associated with some of the charge transfer parameters used in the KMC simulations (e.g., the electronic coupling, dielectric, and reorganization energy). Thus, we performed a sensitivity analysis by conducting the KMC simulations for several choices of the charge transfer parameters to assess the extent to which the observed trend survives changes in the model parameters (Figure S1). This analysis confirms that the mobilities of the 40% and 100% polarity cases are consistently the highest among the systems, whereas the mobility difference between these two cases is small and within the uncertainty of the various parameters.

To understand the relatively constant mobility as the polar side-chain increases, and secondarily, why the 40% and 100% cases show the highest mobility (two times larger than the others), we parsed the distributions of

several key quantities across side-chain compositions and KMC configurations, including the polaron delocalization length, number of trap sites (N_{traps}) , charge transfer rates, pathways per site (N_{paths}) , and electronic couplings (Figure 4). The number of trap sites are defined here as polaron sites for which all outgoing charge transfer rates are $< 100 \text{ ps}^{-1}$, which is slower than the relaxation time of the local structure at most operating temperatures. The trap sites are determined after assigning aggregate states (as described in the methods section), and thus, aggregated sites with exit times > 100 ps are also considered traps. We emphasize that aggregates and trap sites are not synonymous, since aggregation is only based on whether one or more polaron sites exhibit rapid charge exchange. We find a pronounced trend in polaron delocalization length and the number of trap sites (Figure 4B, C). The polaron delocalization length is distinctly smaller for mixed-chain polymers (i.e, 20%-80% polar fraction) and can be attributed to the increased torsional disorder reducing the electronic coupling along the backbone (Figure S3). This also follows from the frustrated packing discussed in the previous section for the mixed-chain polymers. However, the smaller polarons show more uniformity in rate distributions and fewer trap sites (Figure 4C) leading to the nonmonotonic trend with higher mobility for an intermediate polarity of 40%.

In contrast, the higher mobility for the 100% polar case is driven by a combination of higher average charge transfer rates and a better-connected charge transfer network. The 100% polarity case shows the highest mean charge transfer rate out of the simulated systems (Figure 4D). The increased rates are more apparent in the rate distribution (Figure S4), where more interchain pathways $(10^{10} - 10^{13} \text{s}^{-1})$ are seen for the higher polarity cases. This trend is also consistent with the monotonic increase in intersite couplings with the polar side-chain fraction (Figure 4F). The second major driver of increased mobility in the 100% scenario is better connectivity within the charge transfer network. This is quantified in an average sense by the distribution of the number of charge transfer pathways for each polaron site within the network (Figure 4C). With respect to this measure, there is a monotonic increase in the number of pathways (i.e., connections per node using network terminology) as the polar fraction of side-chains increase. These two factors compete with an increasing number of traps as the polarity increases (Figure 4C), with the result that intermediate fractions of polar side-chains exhibit lower mobilities but the homogeneous 100% case consistently shows the highest mobility.

To better quantify the assertion that the charge transport networks are better connected in the more polar systems, we also performed a percolation analysis for the 40%-100% polar side-chain fractions that showed electrolyte swelling. This analysis follows earlier work where the number of distinct subnetworks is parsed based on a charge transfer threshold.⁵⁴ Specifically, polaron sites were aggregated into subnetworks based on their charge transfer rates, such that each site within a network was connected to at least one other site in that network by the stated rate threshold. Since the charge transfer rates for these systems are not symmetric, a site was incorporated in a subnetwork if there existed at least one charge transfer pathway both to and from the polaron site in the cluster. Interestingly, the 40% apolar side-chain fraction shows the smallest number of subnetworks at all values of the rate threshold (Figure 5A), meaning that on average there are more polaron sites in each of its subnetworks. Nevertheless, the spatial extent of the largest charge transport network monotonically increases with polar side-chain fraction (Figure 5B), meaning that while the 40% case has larger networks in terms of the average number of sites per network, they are relatively collapsed and do not effectively percolate the system volume. In contrast, the largest network for the 100% polar sidechain system consistently spans >80% of the system, as

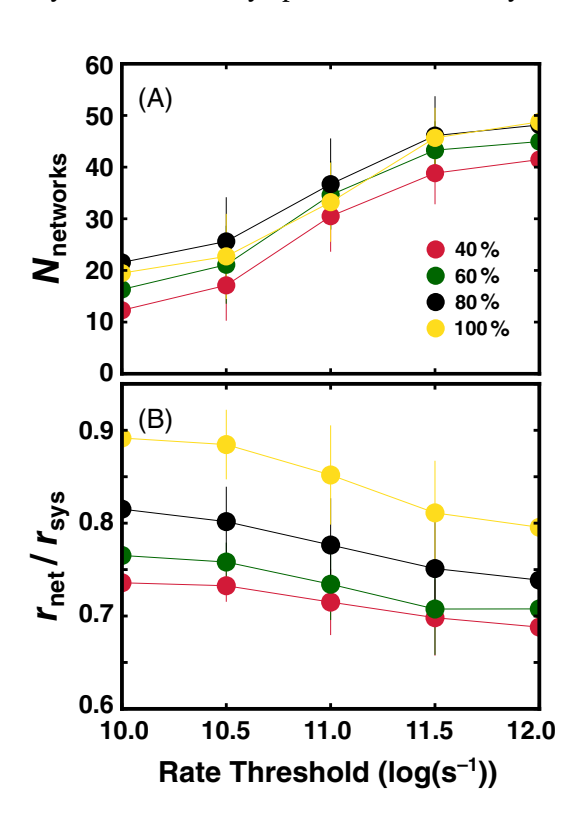


FIGURE 5 The number of distinct subnetworks of polaron sites (A) and the radius of gyration of the largest subnetwork (B) calculated as a function of the side-chain polarity. Subnetworks are defined such that each site is connected to at least one other site within the subnetwork by a rate above the threshold. The radius of gyration of the largest subnetwork is normalized by the radius of gyration the total system $(r_{\text{net}}/r_{\text{sys}})$

measured by its radius of gyration, at all investigated rate thresholds. Thus, the high mobility of the 100% polar system is driven by a combination of higher average charge transfer rates and a more percolative charge transfer network topology.

4 | CONCLUSIONS

The results shown here are consistent with prior experimental observations of the effect of side-chain polarity while providing a detailed picture of the morphology evolution and charge transport. For the random copolymer topology simulated here, we predict that the highest charge mobility would be achieved for the polymers with the highest fraction of polar side-chains. Moreover, since the conductivity is a figure of merit for OMIECs, the increased doping associated with the higher polar side-chain fraction is an additional advantage. Within the limitations of the simulation conditions, there is no advantage to including a mixture of polar and apolar side-chains; whereas, there are several disadvantages, including increased dihedral disorder and reduced interchain charge transfer rates. A key limitation of these simulations is that the fixed water concentration impedes complete chain dissolution, which is a real problem in actual devices. Thus, the guidance resulting from the present simulations are that the polar fraction of side-chains should be increased up to the point that the film does not dissolve in the electrolyte during operation.

The current study has intentionally excluded from consideration the effect of polar side-chain fraction on the doping efficiency. Instead, the doping efficiency was held constant for all cases. This is an important topic for understanding the upper limits of achievable transconductance, for optimizing OMIEC morphology, and designing dopants. Indeed, it is obvious from the current simulations that at high apolar side-chain incorporation that the doping efficiency would necessarily be lower due to limited electrolyte penetration; however, for the intermediate-to-high polar side-chain fractions it is unclear how the changes in polymer-dopant configurations would affect the doping efficiency. This is a phenomenon of consequence for side-chain engineering that subsequent simulations studies could foreseeably resolve.

There are also several side-chain engineering strategies that were not assessed in this study that may have more merit than the mixed random copolymer strategy. For instance, block copolymers with separate contiguous blocks of polar and apolar side-chains may potentially provide control over electrolyte percolation without harming the torsional distributions and polymer connectivity. Likewise, it may be possible to introduce apolar and

polar segments into individual side-chains. Such a strategy is similar to the contemporary apolar linker concept and side-steps the heterogeneity of random copolymers. The current study is also limited with respect to the exploring the degree of hydrophilicity of the side-chains. It is possible that a lower frequency of more hydrophilic side-chains, or alternatively a higher frequency of less hydrophilic side-chains, might be more optimal than the current best-case scenario. The molecular trade-offs involved in these design strategies will be investigated in future studies.

ACKNOWLEDGMENTS

The work performed by Aditi Khot and Brett M. Savoie was made possible by the National Science Foundation (NSF) Division of Chemical, Bioengineering, Environmental, and Transport Systems (CBET) through support provided by the Electrochemical Systems Program (Grant number: 2045887-CBET, Program Manager: Dr Carol Read). Acknowledgment is made to the Donors of the American Chemical Society Petroleum Research Fund for partial support of this research.

ORCID

Brett M. Savoie https://orcid.org/0000-0002-7039-4039

REFERENCES

- B. D. Paulsen, K. Tybrandt, E. Stavrinidou, J. Rivnay, *Nat. Mater.* 2020, 19, 13.
- [2] F. Zhao, Y. Shi, L. Pan, G. Yu, Acc. Chem. Res. 2017, 50, 1734.
- [3] W. Chen, T. Lei, C. Wu, M. Deng, C. Gong, K. Hu, Y. Ma, L. Dai, W. Lv, W. He, X. Liu, Adv. Energy Mater. 2018, 8(10), 1702348.
- [4] G. A. Snook, P. Kao, A. S. Best, J. Power Sources 2011, 196(1), 1.
- [5] J. Rivnay, S. Inal, A. Salleo, R. M. Owens, M. Berggren, G. G. Malliaras, Nat. Rev. Mater. 2018, 3, 1.
- [6] Y. van de Burgt, E. Lubberman, E. J. Fuller, S. T. Keene, G. C. Faria, S. Agarwal, M. J. Marinella, A. A. Talin, A. Salleo, *Nat. Mater.* 2017, 16, 414.
- [7] J. Sunarso, S. Baumann, J. M. Serra, W. A. Meulenberg, S. Liu, Y. S. Lin, J. C. D. Da Costa, J. Membr. Sci. 2008, 320(1–2), 13.
- [8] Q. Zhang, B. Li, S. Huang, H. Nomura, H. Tanaka, C. Adachi, Nat. Photonics 2014, 8, 326.
- [9] G. Wang, A. Morrin, M. Li, N. Liu, X. Luo, J. Mater. Chem. B 2018, 6, 4173.
- [10] H. Wang, M. Barrett, B. Duane, G. Jian, F. Zenhausern, *Mater. Sci. Eng.*, B 2018, 228, 167.
- [11] A. Giovannitti, D.-T. Sbircea, S. Inal, C. B. Nielsen, E. Bandiello, D. A. Hanifi, M. Sessolo, G. G. Malliaras, I. McCulloch, J. Rivnay, *Proc. Natl. Acad. Sci.* 2016, 113, 12017.
- [12] R. Kroon, D. Kiefer, D. Stegerer, L. Yu, M. Sommer, C. Müller, Adv. Mater. 2017, 29, 1700930.
- [13] D. Moia, A. Giovannitti, A. A. Szumska, I. P. Maria, E. Rezasoltani, M. Sachs, M. Schnurr, P. R. F. Barnes, I. McCulloch, J. Nelson, *Energy Environ. Sci.* 2019, 12, 1349.

- [14] J. Liu, L. Qiu, R. Alessandri, X. Qiu, G. Portale, J. J. Dong, W. Talsma, G. Ye, A. A. Sengrian, P. C. T. Souza, M. A. Loi, Adv. Mater. 2018, 30, 1704630.
- [15] X. Chen, A. Marks, B. D. Paulsen, R. Wu, R. B. Rashid, H. Chen, M. Alsufyani, J. Rivnay, I. McCulloch, *Angew. Chem. Int. Ed.* 2021, 60(17), 9368.
- [16] D. Kiefer, A. Giovannitti, H. Sun, T. Biskup, A. Hofmann, M. Koopmans, C. Cendra, S. Weber, L. J. A. Koster, E. Olsson, J. Rivnay, ACS Energy Lett. 2018, 3, 278.
- [17] S. Inal, G. G. Malliaras, J. Rivnay, Nat. Commun. 2017, 8(1), 1.
- [18] A. Giovannitti, I. P. Maria, D. Hanifi, M. J. Donahue, D. Bryant, K. J. Barth, B. E. Makdah, A. Savva, D. Moia, M. Zetek, P. R. Barnes, *Chem. Mater.* 2018, 30, 2945.
- [19] A. Savva, R. Hallani, C. Cendra, J. Surgailis, T. C. Hidalgo, S. Wustoni, R. Sheelamanthula, X. Chen, M. Kirkus, A. Giovannitti, A. Salleo, Adv. Funct. Mater. 2020, 30(11), 1907657.
- [20] Anna M Österholm, James F Ponder Jr, M. De Keersmaecker, D Eric Shen, and John R Reynolds. *Chem. Mater.*, 31:2971– 2982. 2019.
- [21] S. L. Pittelli, M. De Keersmaecker, J. F. Ponder Jr., A. M. Österholm, M. A. Ochieng, J. R. Reynolds, J. Mater. Chem. C 2020, 8, 683.
- [22] M. Moser, T. C. Hidalgo, J. Surgailis, J. Gladisch, S. Ghosh, R. Sheelamanthula, Q. Thiburce, A. Giovannitti, A. Salleo, N. Gasparini, A. Wadsworth, Adv. Mater. 2020, 32, 2002748.
- [23] M. Moser, L. R. Savagian, A. Savva, M. Matta, J. F. Ponder Jr., T. C. Hidalgo, D. Ohayon, R. Hallani, M. Reisjalali, A. Troisi, A. Wadsworth, *Chem. Mater.* 2020, 32(15), 6618.
- [24] R. K. Hallani, B. D. Paulsen, A. J. Petty, R. Sheelamanthula, M. Moser, K. J. Thorley, W. Sohn, R. B. Rashid, A. Savva, S. Moro, J. P. Parker, J. Am. Chem. Soc. 2021, 143, 11007.
- [25] B. X. Dong, C. Nowak, J. W. Onorato, J. Strzalka, F. A. Escobedo, C. K. Luscombe, P. F. Nealey, S. N. Patel, *Chem. Mater.* 2019, 31, 1418.
- [26] P. Schmode, A. Savva, R. Kahl, D. Ohayon, F. Meichsner, O. Dolynchuk, T. Thurn-Albrecht, S. Inal, M. Thelakkat, ACS Appl. Mater. Interfaces 2020, 12(11), 13029.
- [27] I. P. Maria, B. D. Paulsen, A. Savva, D. Ohayon, R. Wu, R. Hallani, A. Basu, W. Du, T. D. Anthopoulos, S. Inal, J. Rivnay, Adv. Funct. Mater. 2021, 31(14), 2008718.
- [28] D. Ohayon, A. Savva, D. Weiyuan, B. D. Paulsen, I. Uguz, R. S. Ashraf, J. Rivnay, I. McCulloch, S. Inal, ACS Appl. Mater. Interfaces 2021, 13, 4253.
- [29] T. Nicolini, J. Surgailis, A. Savva, A. D. Scaccabarozzi, R. Nakar, D. Thuau, G. Wantz, L. J. Richter, O. Dautel, G. Hadziioannou, N. Stingelin, Adv. Mater. 2021, 33, 2005723.
- [30] J. Surgailis, A. Savva, V. Druet, B. D. Paulsen, R. Wu, A. Hamidi-Sakr, D. Ohayon, G. Nikiforidis, X. Chen, I. McCulloch, J. Rivnay, Adv. Funct. Mater. 2021, 31, 2010165.
- [31] I. Sahalianov, J. Hynynen, S. Barlow, S. R. Marder, C. Müller, I. Zozoulenko, J. Phys. Chem. B 2020, 124, 11280.
- [32] M. Moser, J. Gladisch, S. Ghosh, T. C. Hidalgo, J. F. Ponder Jr.., R. Sheelamanthula, Q. Thiburce, N. Gasparini, A.

- Wadsworth, A. Salleo, S. Inal, Adv. Funct. Mater. 2021, 31(26), 2100723.
- [33] A. Khot, B. M. Savoie, Macromolecules 2021, 54, 4889.
- [34] S. J. Marrink, H. J. Risselada, S. Yefimov, D. P. Tieleman, A. H. De Vries, J. Phys. Chem. B 2007, 111, 7812.
- [35] S. O. Yesylevskyy, L. V. Schäfer, D. Sengupta, S. J. Marrink, PLoS Comput. Biol. 2010, 6, e1000810.
- [36] R. Alessandri, J. J. Uusitalo, A. H. de Vries, R. W. A. Havenith, S. J. Marrink, J. Am. Chem. Soc. 2017, 139(10), 3697.
- [37] F. Grunewald, G. Rossi, A. H. De Vries, S. J. Marrink, L. Monticelli, J. Phys. Chem. B 2018, 122, 7436.
- [38] R. Berardi, C. Fava, C. Zannoni, Chem. Phys. Lett. 1998, 297(1-2), 8.
- [39] B. Kuei, E. D. Gomez, Soft Matter 2017, 13(1), 49.
- [40] M. H. Abraham, H. S. Chadha, G. S. Whiting, R. C. Mitchell, J. Pharm. Sci. 1994, 83, 1085.
- [41] L. Q. Flagg, C. G. Bischak, J. W. Onorato, R. B. Rashid, C. K. Luscombe, D. S. Ginger, J. Am. Chem. Soc. 2019, 141(10), 4345.
- [42] S. Plimpton, J. Comput. Phys. 1995, 117(1), 1.
- [43] M. Modarresi, J. F. Franco-Gonzalez, I. Zozoulenko, Phys. Chem. Chem. Phys. 2018, 20, 17188.
- [44] G. J. Martyna, D. J. Tobias, M. L. Klein, J. Chem. Phys. 1994, 101, 4177.
- [45] S. J. Plimpton, W. M. Brown, M. K. Petersen, G. S. Grest, J. Chem. Phys. 2009, 130, 044901.
- [46] J.-P. Ryckaert, G. Ciccotti, H. J. C. Berendsen, J. Comput. Phys. 1977, 23, 327.
- [47] A. Stukowski, Modell. Simul. Mater. Sci. Eng. 2009, 18(1), 015012.
- [48] R. A. Marcus, Rev. Mod. Phys. 1993, 65, 599.
- [49] V. Rühle, J. Kirkpatrick, D. Andrienko, J. Chem. Phys. 2010, 132(13), 134103.
- [50] F. C. Grozema, P. T. Van Duijnen, Y. A. Berlin, M. A. Ratner, L. D. A. Siebbeles, *J. Phys. Chem. B* 2002, 106, 7791.
- [51] P. F. Barbara, T. J. Meyer, M. A. Ratner, J. Phys. Chem. 1996, 100, 13148.
- [52] S. S. Zade, N. Zamoshchik, M. Bendikov, Acc. Chem. Res. 2011, 44(1), 14.
- [53] T. Brereton, O. Stenzel, B. Baumeier, D. Andrienko, V. Schmidt, D. Kroese, Methodol. Comput. Appl. Probab. 2014, 16, 465.
- [54] B. M. Savoie, K. L. Kohlstedt, N. E. Jackson, L. X. Chen, M. O. De La Cruz, G. C. Schatz, T. J. Marks, M. A. Ratner, *Proc. Natl. Acad. Sci.* 2014, 111, 10055.

SUPPORTING INFORMATION

Additional supporting information may be found in the online version of the article at the publisher's website.

How to cite this article: A. Khot, B. M. Savoie, *J. Polym. Sci.* **2021**, 1. https://doi.org/10.1002/pol.20210773

How Side-Chain Hydrophilicity Modulates

Morphology and Charge Transport in Mixed

Conducting Polymers

Aditi Khot and Brett M. Savoie*

Davidson School of Chemical Engineering, Purdue University, West Lafayette, IN, 47906

E-mail: bsavoie@purdue.edu

Phone: 765-494-4235

Supporting Information 1

1.1 Parameters for Non-bonded and Bonded potentials

The LJ parameters used in the simulations are listed in Table S1 and on the corresponding Martini

bead type. The Gay-Berne parameters are specified according to the LAMMPS notation. The

parameters for the Gay-Berne interactions are unchanged from our previous publication, but the y

and z axes parameters have been interchanged to comply with the original Gay-Berne functional

form. 1 Note that this modification only alters the energy coefficient by a factor of 0.91 and has

no significant affect on the physics of the system. The intramolecular parameters used for the

simulations are listed in Table S2.

1

Table S1: Parameters used for non-bonded interactions in the simulations. Units of all parameters are consistent with LAMMPS 'real' units (kcal mol⁻¹, Å etc.) and potential styles. The bead-type for backbone, polar sidechain, apolar sidechain, and chloroform are C4, EO, SC3 and C4, respectively. Water is made of POL, WM, and WP beads, from which the beads WM and WP do not experience any Van der Waal interactions. The interaction of backbone bead with other backbone beads is modelled as Gay-Berne potential (and not C4-C4 interaction) and the parameter values are reported next to "B-B".

B-B	$\sigma_x = \sigma_y = 5.0$, $\varepsilon_x = \varepsilon_y = 0.25$, $\sigma_z = 3.0$, $\varepsilon_z = 1.2$, $\sigma_c = 3.0$					
	C4	EO	SC3	POL	Qa	
C4	$\varepsilon = 0.84, \sigma = 4.7$	$\varepsilon = 0.70, \sigma = 4.7$	$\varepsilon = 0.84, \sigma = 4.7$	$\varepsilon = 0.61, \sigma = 4.7$	$\varepsilon = 0.74, \sigma = 4.7$	
EO		$\varepsilon = 0.61, \sigma = 4.3$	$\varepsilon = 0.53, \sigma = 4.3$	$\varepsilon = 0.79, \sigma = 4.7$	$\varepsilon = 0.84, \sigma = 4.7$	
SC3			$\varepsilon = 0.63, \sigma = 4.3$	$\varepsilon = 0.61, \sigma = 4.7$	$\varepsilon = 0.65, \sigma = 4.3$	
POL				$\varepsilon = 0.96, \sigma = 4.7$	$\varepsilon = 1.19, \sigma = 4.7$	
Qa					$\varepsilon = 0.84, \sigma = 4.7$	

Table S2: Parameters used for bonded interactions in the simulations. Units of all parameters are consistent with LAMMPS 'real' units (kcal mol⁻¹, Å etc.) and potential styles. The bonds in water molecules between the WM-POL and WP-POL beads are constrained using the SHAKE algorithm.²

Bono	ds	Angles				
В-В	$k = 25.0, r_0 = 4.3$	B-B-B	$k = 1.0, \theta_0 = 160.0$			
B-SP(SA)	$k = 1.5, r_0 = 4.7$	B-B-SP(SA)	$k = 3.0, \theta_0 = 90.0$			
SP-SP	$k = 8.35, r_0 = 3.22$	B-SP(SA)-SP(SA)	$k = 3.0, \theta_0 = 180.0$			
SA-SA	$k = 1.5, r_0 = 3.6$	SP-SP-SP	$k = 6.0, \theta_0 = 135.0$			
POL-WM	$r_0 = 1.4$	SA-SA-SA	$k = 3.0, \theta_0 = 180.0$			
POL-WP	$r_0 = 1.4$	WM-POL-WP	$k = 0.5019, \ \theta_0 = 0.0$			
Dihed	rals	Additional Potentials				
B-B-B-B	$k_1 = 0.5, k_2 = 0.6,$	B-B, <i>d</i>	$k_1 = 0.0, k_2 = 2.0, k_3 = 0.0, k_4 = 0.0$			
	$k_3 = 0.0, k_4 = 0.0$					
SP(SA)-B-B-SP(SA)	$k_1 = 3.0, k_2 = 0.0,$	B-B, <i>a</i> ₁	$k_a = 7.5, \theta_0 = 90.0$			
	$k_3 = 0.0, k_4 = 0.0$					
		B-B, <i>a</i> ₂	$k_a = 7.5, \theta_0 = 90.0$			
		B-SP(SA), a	$k_a = 3.0, \theta_0 = 90.0$			

1.2 Parameters for Charge Transport Simulations

The following parameters were used for the Marcus expressions discussed in the main text: $J_{\text{inter}} = 0.01 \text{ eV}$, $r_0 = 3.5 \text{ Å}$, $\alpha = 0.8 \text{ Å}^{-1}$, $J_{\text{intra}} = 0.31 \text{ eV}$, $\varepsilon_{\text{opt}} = 3$, and $\varepsilon_s = 10$. The expressions for external reorganization, λ , and oxidation energy, E, as a function of oligomer length, l, were obtained from fits to reported data for polythiophene.³ The governing expression for the external reorganization energy as a function of l is

$$\lambda = \begin{cases} -0.0973\sqrt{l} + 0.4922, & \text{if } l \le 15\\ \frac{1.9489}{l} - 0.0092, & \text{otherwise} \end{cases}.$$

The governing expression for the oxidation energy as a function of l is

$$E = 4.1336 l^{-0.75} + 4.67.$$

1.3 Sensitivity Analysis of KMC Simulations

To assess the impact of the charge transport parameters on the results of the KMC simulations, the simulations were rerun with single factor sensitivity analysis. Specifically, a positive and negative deviation from the values used in the main text simulations was performed for each variable, including the intermolecular coupling decay rate ($\beta = 0.6 \text{ Å}^{-1}$ and 1.0 Å^{-1} are the low and high values, respectively), reference intermolecular coupling strength ($J_{\text{inter}} = 0.005 \text{ eV}$ and 0.02 eV), delocalization length dependence of the HOMO energy level (E+ and E- modeled as $3.1l^{-0.75}+4.67$ eV and $5.167l^{-0.75}+4.67$ eV, respectively), and the dielectric constant ($\epsilon = 7.5$ and 12.5) while keeping the other parameters at their mean value (Fig. S1).

For all cases, we observe a mobilities within approximately the same order of magnitude for all side-chain polarities. When parameters are selected that increase the mean charge transport rate (e.g., by increasing the reference coupling J_{inter} , decreasing the coupling decay rate β , or reducing the HOMO energy level decay), we observe the expected increase in mobility, while

still observing a non-monotonic trend in the mobility across side-chain polarity composition. The mobility at 100% polarity also increases and becomes predominant compared to the other cases as the charge transport rate increases (Fig. S1a-b). This corroborates the previous explanation that the mobility is higher at 100% side-chain polarity due to the faster charge transport rate. The the length-dependence of the HOMO energies (Fig. S1c) more strongly impacts the 40% case than 100% as the latter has longer polaron sites for which posses similar HOMO energies across all three HOMO energy curves tested. Interestingly, we find the mobility to be highest for an intermediate dielectric of 10. Increasing the dielectric constant increases the reorganization energy for charge transfer while reducing the electrostatically induced energy disorder. We refrain from overinterpreting this result, since the treatment of a spatially constant dielectric is already a strong, albeit common, approximation. However we note that both beneficial effects could be achieved by locally reducing the dielectric along the backbone, which is similar to the contemporary strategy of adding an apolar linking group at the base of the side-chain.

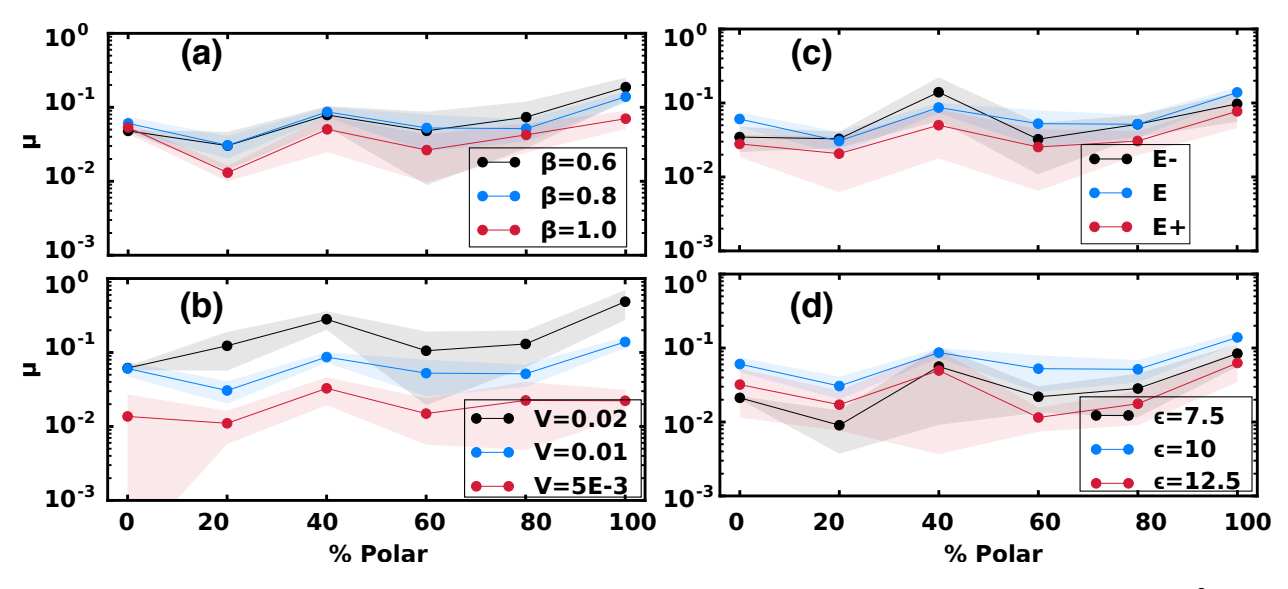


Figure S1: Single factor sensitivity analysis of the KMC simulation results for mobility (cm²/Vs) as a function of different side-chain compositions. The effect of the intermolecular coupling decay rate (β [Å⁻¹]; panel a), the reference intermolecular coupling strength (J_{inter} [eV];b), delocalization length dependence of the HOMO energy level (E;c), and the dielectric constant (ε ;d) are shown in the corresponding panels.

1.4 Additional Figures Referenced in the Main Text

In the main text we reported the superlinear swelling of the polymer with respect to the polar side-chain percentage (Fig. 2 in the main text). In Figure S2 we report several corroborating datasets that were parsed from the CG-MD trajectories, including the net volume of the swelled polymer at each sidechain composition (Fig. S2a), the water-water radial distribution function (rdf; Fig S2b), and the polymer backbone-ion rdf (Fig. S2c). The onset of water percolation at 40% polar side-chains followed by superlinear growth is clearly visible from the polymer volumes. Likewise, electrolyte percolation is accompanied by a reduction in bulk water concentration, as evidenced by the monotonic decay in the height of the first peak in the water-water rdf with increasing polar side-chain fraction. The onset of percolation is even more clearly observed in the monotonic increase in the first peak of the ion-backbone rdf with polar side-chain fraction, and the large jump between the 20% and 40% curves. The polymers show very weak lamellar packing for all polar side-chain fractions (Fig. S2d) evidenced by a small peak around 17 Å. This is approximately twice the side-chain length, meaning there is very little interdigitation of the chains, and this lamellar packing is further suppressed as electrolyte enters the polymer film.

As reported in the main text, polaron delocalization is significantly affected by the polar side-chain fraction. This is also reflected in the intramolecular coupling distributions (Fig. S3), which skew to the lowest values for the 40% case. We ascribe this to the increased torsional disorder caused by side-chain heterogeneity.

The distribution of rates between polaronic sites are reported below before (Fig. S4a) and after (Fig. S4b) incorporating the effect of polaron site aggregates. The higher rates of $> 10^{13} \rm s^{-1}$ represent the relatively fast transport between localized polarons along the same chain and appear similar for all side-chain compositions before including the effect of aggregates. In contrast, the interchain rates $10^{12} - 10^{13} \rm s^{-1}$ are faster for more polar cases due to the improved packing. After aggregating sites where most time is spent, the fast and slow pathways decrease and increase, respectively for the 100% polar case. Note that the intrachain rates above the polaron threshold of $10^{14} \rm s^{-1}$ represent pairs of intrachain sites where the rate is faster one way than the reverse due to

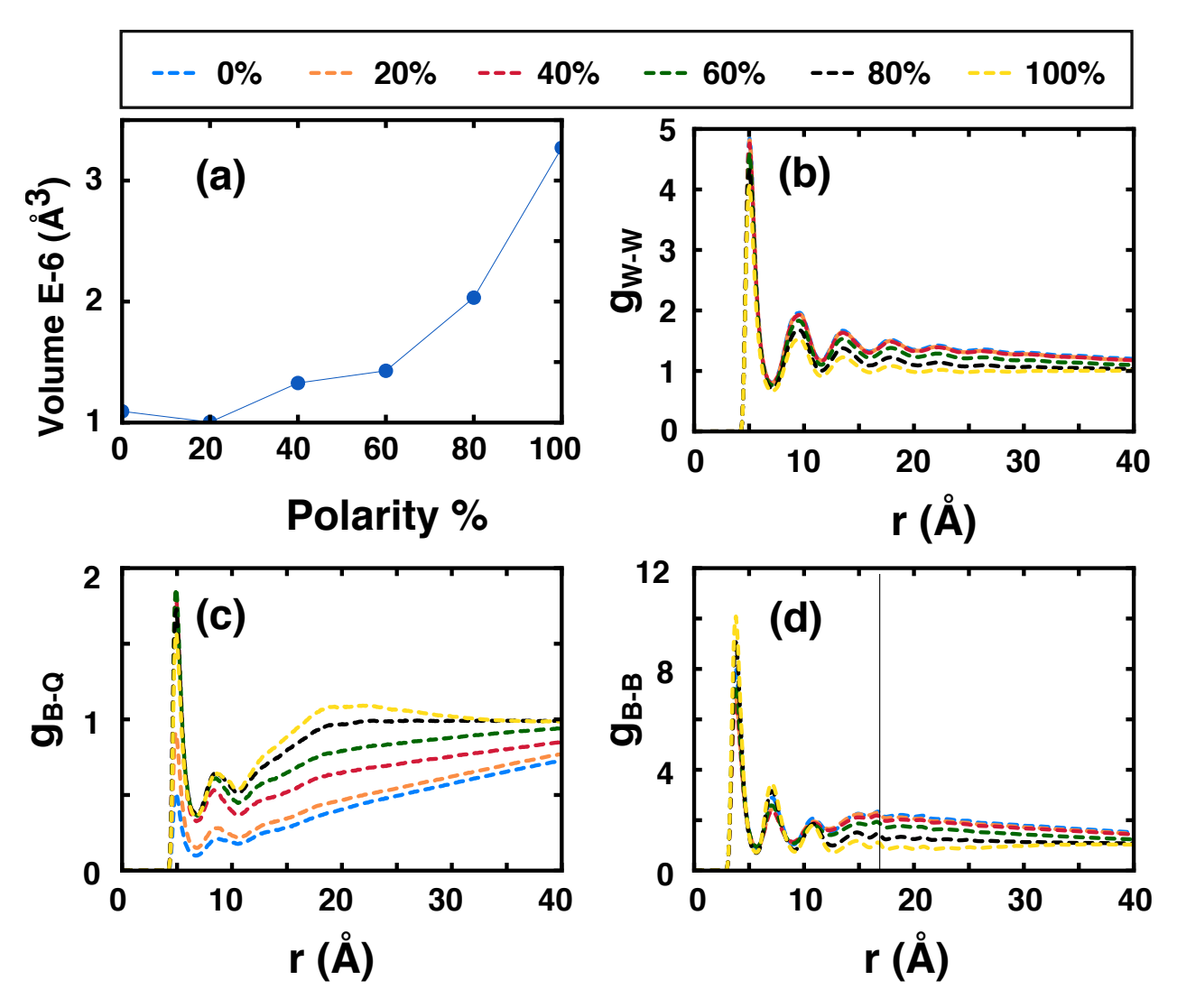


Figure S2: (a) The approximate volume of the swelled polymer as calculated from the convex hull of the polymer coordinates parsed from the CG-MD trajectories. (b) The water-water radial distribution function (rdf) as a function of the polar fraction of side-chains. (c) The backbone-ion rdf as a function of the polar fraction of side-chains (d) The backbone-backbone rdf, with the weak lamellar packing around 17 Åindicated by a vertical line.

electrostatic disorder.

For completeness, the distributions for the reorganization energy (λ) and site energy differences (ΔE) of charge transfer are also reported in Figure S5. As pointed out in the main text, the interchain rate increases with polarity due to improved electronic coupling. The reorganization energy decreases with polarity from 40-100%, due to the increase in polaron delocalization length with increasing side-chain polarity. This trend also partially explains the increase in the mean

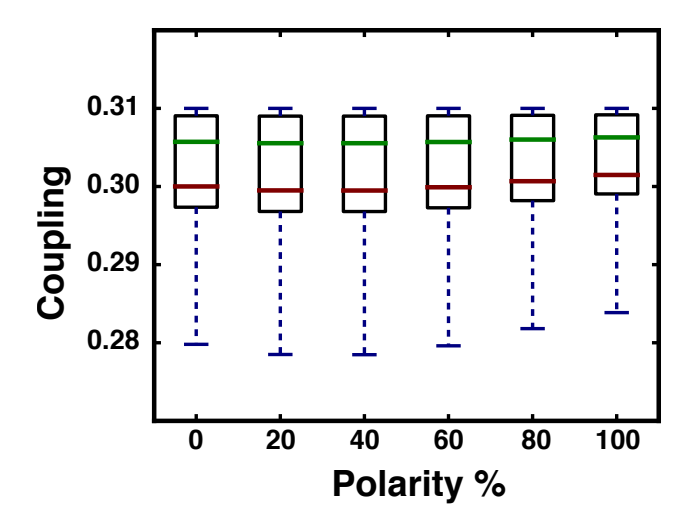


Figure S3: Distributions of the intramolecular couplings between polaron sites for different sidechain compositions. The green and red lines indicate the median and mean, respectively.

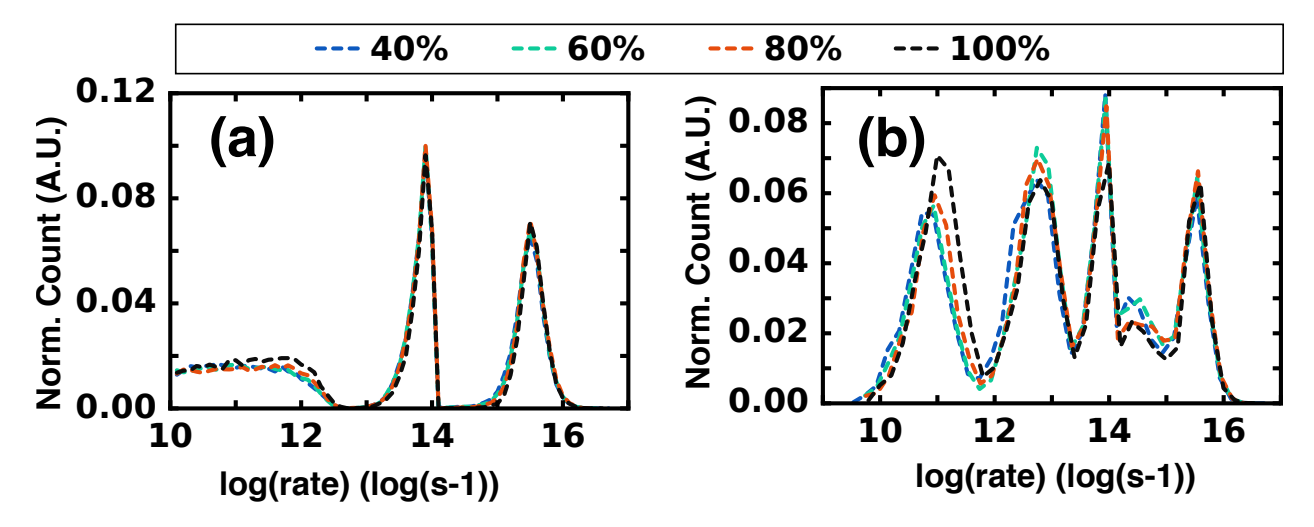


Figure S4: Distributions of the polaronic site charge transfer rates (a) before and (b) after incorporating the effect of aggregates.

charge transfer rate with the polar side-chain fraction. There is not a significant correlation between the energies and the observed mobilities with the exception that the 100% polar side-chain scenario shows the lowest average site disorder.

Ion mobility (Fig. S6) is another important figure of merit for mixed conductor systems. Although the ion mobility is easy to parse from the CG-MD simulations, the interpretation is confounded by the presence of bulk electrolyte in the simulations with low polar side-chain fractions. Specifically, between 0-60% polar side-chain fractions, bulk electrolyte is still present in the simulations which results in the highest ion mobilities in these scenarios. This is caused by the fact that

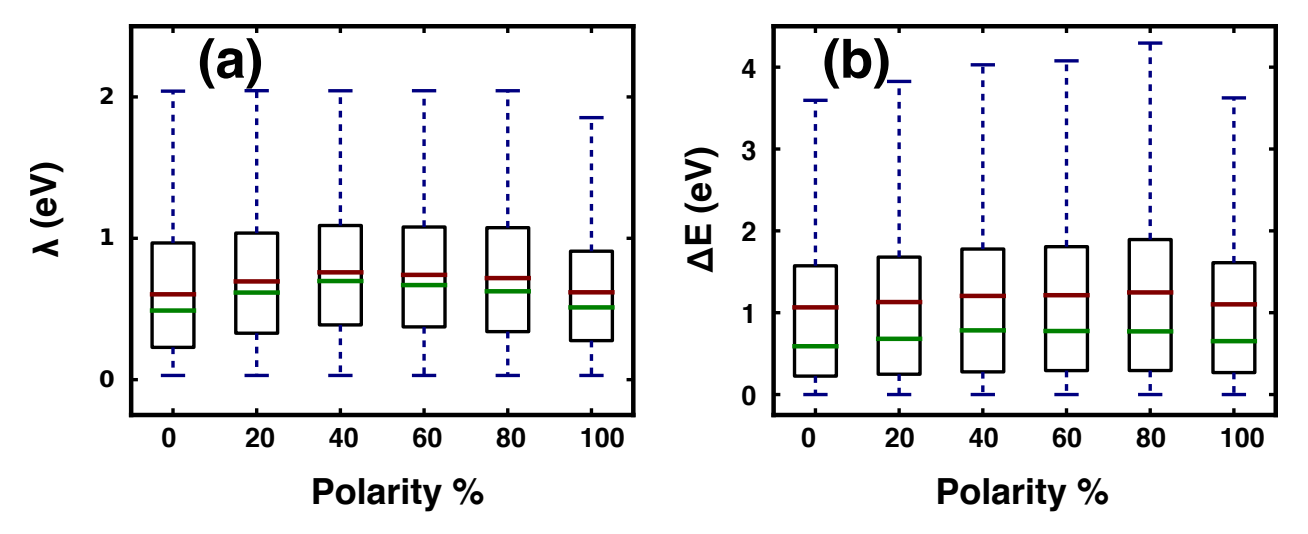


Figure S5: Distribution of (a) reorganization energy and (b) energy differences between polaron sites across different side-chain compositions. The green and red lines indicate the median and mean, respectively.

all of the simulations were equilibrated with sufficient electrolyte to saturate the polymer, leading to bulk electrolyte still existing in the cases of high apolar side-chain loadings and partial percolation. For this reason we have included these results for completeness, but have not significantly discussed them in the main text.

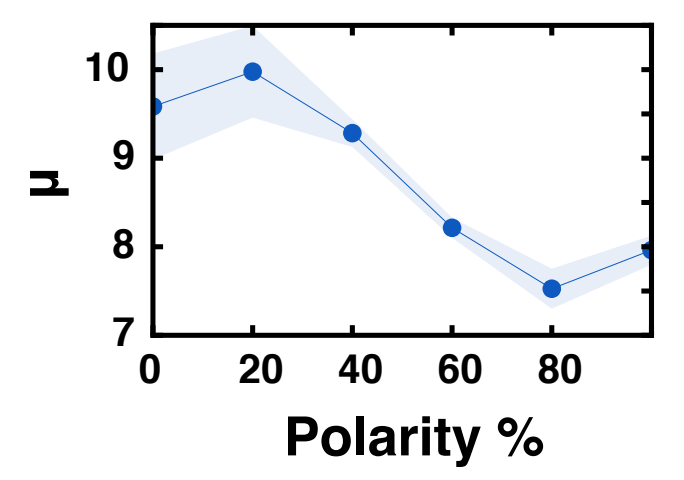


Figure S6: The ion mobility $(x10^{-5} \text{cm}^2/\text{Vs})$ as a function of side-chain composition. These mobilities were parsed from the CG-MD simulations based on the ionic mean-squared displacements versus time and using the Einstein relation. The standard errors across the trajectories are reported as the shaded regions.

References

- (1) Berardi, R.; Fava, C.; Zannoni, C. A Gay–Berne potential for dissimilar biaxial particles. *Chemical physics letters* **1998**, 297, 8–14.
- (2) Ryckaert, J.-P.; Ciccotti, G.; Berendsen, H. J. Numerical integration of the cartesian equations of motion of a system with constraints: molecular dynamics of n-alkanes. *Journal of computational physics* **1977**, *23*, 327–341.
- (3) Zade, S. S.; Zamoshchik, N.; Bendikov, M. From short conjugated oligomers to conjugated polymers. Lessons from studies on long conjugated oligomers. *Accounts of Chemical Research* **2011**, *44*, 14–24.